Bipolar device fabrication using a scanning tunneling microscope

Tomáš Škereň,[1] Sigrun A. Köster,[1] Bastien Douhard,[2]

Claudia Fleischmann,[2] and Andreas Fuhrer[1, *]

[1]*IBM Research – Zürich, Säumerstrasse 4, 8803 Rüschlikon, Switzerland*

[2]*IMEC, Kapeldreef 75, 3001 Heverlee, Belgium*

Abstract

Hydrogen resist lithography with the tip of a scanning tunneling microscope (STM) can be used to fabricate atomic-scale dopant devices in silicon substrates and could potentially be used to build a dopant-based quantum computer. However, all devices fabricated so far have been based on the n-type dopant precursor phosphine. Here, we show that diborane can be used as p-type dopant precursor, allowing p-type and bipolar dopant devices to be created. Characterisation of diborane δ-layers reveals that similar mobilities and densities can be achieved as for phosphine, with sheet resistivities as low as 300 Ω. STM imaging and transport measurements of a 5.5-nm-wide p-type dopant nanowire give an estimated upper bound of 2 nm for the lithographic resolution of the p-type dopant profiles. By combining our p-type doping approach with established phosphine-based n-type doping, we fabricate a 100 nm wide pn-junction and show that its electrical behaviour is similar to that of an Esaki diode.

Conventional semiconductor devices can today be fabricated with dimensions of only a few nanometers, but achieving atomically-sharp dopant profiles remains challenging [29–32]. Limits in achievable doping densities, as well as unwanted diffusion of dopants from the leads to the channel, impact the access resistance and variability of devices. Single dopants, on the other hand, can be used as artificial atoms, and, embedded in near perfect crystalline semiconductors, can create qubits [33] and charge pumps [34]. Hydrogen-resist lithography, in combination with a scanning tunnelling microscope (STM), can achieve both atomically sharp dopant profiles [35] and deterministic patterning of single dopant devices [36].

Hydrogen passivation of a clean Si(001) surface with mono hydride strongly suppresses surface reactivity. Local removal of this hydrogen resist layer with the tip of an STM in ultra-high vacuum creates reaction sites on the silicon surface (dangling bonds). In these patterned regions, gas phase dopant precursors such as phosphine or diborane can attach and be incorporated into substitutional silicon sites by a short anneal, which can then be followed by overgrowth with silicon. As a result, hydrogen-resist lithography can create atomically-precise planar dopant devices in the host silicon crystal.

For phosphine, this process is well established and low temperature device fabrication is possible without significant blurring (diffusion) of the dopant structures [37]. However, δ-doped p-type devices have not been explored so far with this technique. The nanoscale patterning of acceptor structures is crucial for the development of p-type field-effect transistors using such STM fabrication methods, as well as the fabrication of bipolar planar dopant devices and the ability to exploit electric field tunability of acceptor spin states for spin manipulation [38]. In this Article, we report acceptor device fabrication with the STM using gas-phase δ-doping with diborane (B_2H_6) as a dopant precursor.

In order to achieve STM-based dopant device fabrication using diborane as a gas-phase dopant, a number of fundamental requirements need to be fulfilled. First, conditions for the reaction of diborane with the Si surface need to be determined; silicon surfaces exposed to diborane gas should become saturated with dopant precursor molecules, while avoiding unintentional passivation with hydrogen which is present as a carrier gas. Second, hydrogen passivated Si surfaces should prevent surface reactions with diborane leading to the required selectivity of the hydrogen resist. Finally, it is important to confirm that the boron δ-layer can be overgrown with epitaxial Si without segregation of the boron atoms to the surface during silicon epitaxy. Thus, we first investigate the validity of these conditions, and then

explore the electrical transport properties of boron doped δ-layers and their dependence on diborane dose and activation temperature. These results are then used to demonstrate STM-based device fabrication and the creation of a p-type nanowire and a bipolar pn-junction.
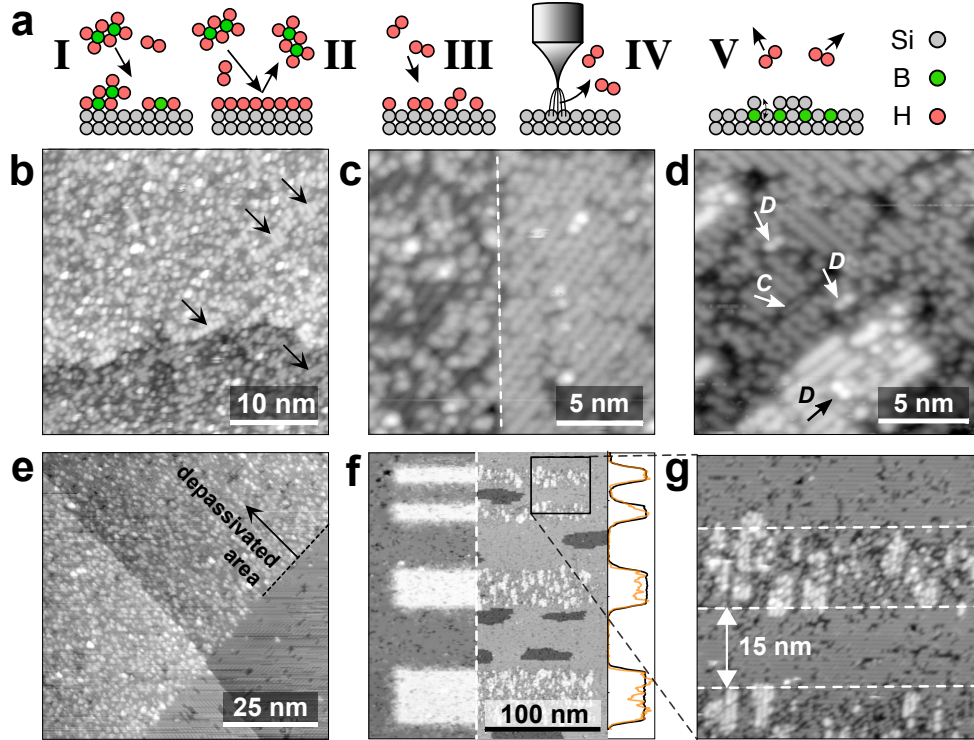

FIG. 1. | **Adsorption and surface reactions of diborane with the Si(001) and H:Si(001) surface. a** Schematic depiction of the different process steps. **b** STM image of the Si(001) surface prepared by flash annealing in UHV after exposure to 3 L of diborane (30% in H_2) at 200 °C. **c** Si surface exposed to 230 L of pure H_2 under similar conditions as in **b**. The right half was subsequently desorbed using the STM. **d** The surface shown in **b** after annealing at 510 °C for 5 min. C and D denote features related to boron in the silicon surface. **e** Edge of an STM-desorbed patch after exposure to 90 L of diborane at 180 °C. **f** Four desorbed stripes before diborane exposure (left part) and after exposure to 90 L of diborane at 180 °C plus a subsequent incorporation anneal for 1 min at 510 °C (right part). The line traces on the right edge of the image show averaged line-cuts of the stripes before (black) and after (brown) incorporation. **g** Higher resolution image of the narrowest stripes in **f**.

Gas-phase δ-doping with diborane

A diborane molecule impinging on the clean silicon surface can break into fragments and react with available silicon surface bonds (see **I**, Fig. 1 **a**). Previous work has shown that saturation of the Si(001) surface with diborane requires extremely high doses of up to 1000 L [39, 40]. Heating of the silicon substrate allows diborane molecules to react more easily, thus reducing the required diborane dose. However, we want to limit temperatures to below 450 °C such that the hydrogen resist remains intact [41] and prevents the reaction of diborane with the surface (see **II**, Fig. 1 **a**). Furthermore, while molecular hydrogen (the carrier gas) does not stick to the silicon surface at room temperature, unwanted surface reaction of H_2 increases with temperature [42] (see **III**, Fig. 1 **a**). We therefore choose a sample temperature of 200 °C during diborane dosing. This ensures that patterns in the hydrogen resist stay intact and exposed Si(001) surfaces reach acceptable doping densities.

Figure 1 **b** shows a filled state STM image of a bare silicon surface after exposure to 3 L of diborane at 200 °C (see Methods for details about dose interpretation). The image spans two atomic silicon steps and on each we observe three distinct levels in the topography. At the intermediate level residual dimer from the usual 2x1 reconstructed silicon (100) surface are observed (see arrows). Furthermore, there are both darker depressions and brighter protrusions. The dark areas can be identified as the parts of the silicon surface that are hydrogen passivated. Here, both the carrier gas H_2 and the diborane molecule B_2H_6 are potential sources of surface hydrogen. Furthermore, it has previously been suggested that some boron hydride fragments may appear similar to a hydrogenated silicon dimer [43] and would therefore also appear darker here.

As with phosphine [44], the maximum achievable boron density through gas-phase doping is expected to be limited by unintentional surface passivation with hydrogen present in B_2H_6 [39]. In other words, breakdown of the diborane molecule on the silicon surface will also passivate some of the available reaction sites with hydrogen and thus reduce the density of the diborane precursor fragments that can attach (see **I**). Here, the H_2 carrier gas may lead to additional unwanted passivation of surface sites [42]. To clarify this, the silicon surface shown in Figure 1 **c** was exposed to 230 L of pure molecular hydrogen at 220 °C. We find that about half of the surface is covered by hydrogen through surface reactions, as shown in the left part of the STM image (see **III** in Fig. 1 **a**). On the right side the hydrogen

was subsequently desorbed using the STM tip (see **IV** in Fig. 1 **a**). This suggests that only a negligible fraction of the hydrogen in Figure 1 **b**, with a 20x lower dose, originates from the H_2 carrier gas, justifying our choice of $200\,°C$ as a dosing temperature.

After dosing we anneal the sample to incorporate the boron into the silicon surface. During this process we want to avoid that boron containing species leave the surface and are lost for the dopant nanostructure. Thermal decomposition studies suggest that only hydrogen desorbs into the gas-phase while boron remains on the surface and incorporates into substitutional sites at temperatures above $400\,°C$ [40] (see **V** in Fig. 1 **a**). Figure 1 **d** shows an image of the surface in 1 **b** after annealing to $510\,°C$ for $5\,min$. Here, we can identify several features which have been attributed to boron atoms in the surface, namely a double dot protrusion marked D and an arrangement of indented atoms marked C. Both have been discussed before for samples annealed at similar temperatures [39, 43, 45]. While the C feature is not easy to identify, the D feature seems to be typical for substitutional boron on Si(001) replacing one of the two Si surface dimer atoms at low boron density [45]. In addition to this, there are still several depressions which we attribute to strain induced defects in the silicon surface. These STM images show that B_2H_6 adsorbs on the silicon surface at $200\,°C$ and boron is at least partially incorporated into the silicon crystal after further annealing. More precise quantification of the effect of the incorporation anneal is obtained from transport measurements on boron δ-layers in the next section.

Selectivity of the hydrogen resist towards diborane dosing is demonstrated in Figure 1 **e**. It shows the boundary of an area that was depassivated using the STM tip and exposed to $90\,L$ of diborane. In the depassivated region (top left) the diborane clearly attaches to the silicon surface while the hydrogen passivated area (bottom right) remains pristinely clean with a sharply defined border on the nanometer scale. Such an STM defined pattern remains stable even after annealing at temperatures T_A high enough to desorb the hydrogen resist. Figure 1 **f** shows a pattern of four STM defined patches dosed with $90\,L$ of diborane at $180\,°C$ after a $1\,min$ anneal to $T_A = 510\,°C$. Even though clear changes in surface morphology occur, the stripes are still well resolved. The dark islands represent the next Si layer below the surface. They are visible everywhere on the sample surface and are most likely caused by etching during the removal of hydrogen. In the regions exposed to diborane we find bright agglomerates which show dimer row formation as can be seen in the zoom in Figure 1 **g**. We believe this to be ejected silicon atoms that have exchanged place with incorporated boron

and start to form islands due to diffusion. While it is difficult to clearly identify the boron, it is fair to assume that the incorporated boron atoms diffuse much less than the ejected silicon on the surface. This means that even at $T_A = 510\,°C$, the resolution of p-type dopant device patterning is expected to be significantly better than $2\,nm$. This is further supported by the good overlap of the two line-traces in 1 **f** which are horizontally averaged line cuts of the four patches before and after annealing (arbitrarily scaled in z).

Si overgrowth of a δ-doped structure can be accompanied by segregation of dopant atoms towards the surface during overgrowth. This was found to be an issue in the case of phosphine δ-layers and can lead to blurring of the vertical δ-doping profile or, ultimately, also deterioration of the in-plane resolution [46]. For phosphorus doping, this problem was addressed by using a so-called locking layer i.e. the first few monolayers of the Si encapsulation layer are grown at lower temperature to suppress segregation while the rest of the overgrowth is performed at an elevated temperature in order to preserve the crystalline quality of the capping layer and decrease the number of defects [47].

In boron δ-doped layers we find that segregation is less of a concern. Secondary ion mass spectroscopy (SIMS) measurements were performed on two samples: S1 (default preparation as shown in Fig. 2 **a**) and S2 (includes locking-layer as shown in Fig. 2 **b**). SIMS traces for ^{11}B (solid lines) and ^{10}B (dashed lines) are shown in Figs. 2 **c** (linear scale) and 2 **d** (logarithmic scale) with the correct isotopic ratio and for both samples. In both cases the leading edge (left side) of the SIMS profile has a slightly smaller slope indicating that there is some boron segregation during overgrowth. This is stronger for the trace of sample S1 (blue trace) which exhibits a shoulder towards the surface. This means that the locking layer can indeed also improve the sharpness of the boron δ-doping profile, however, the measured characteristics are very similar for both samples and, compared to phosphorus doping, segregation of the dopants does not represent a substantial issue. Furthermore, a FWHM of $1.4\,nm$ for the δ-layer thickness is already close to the theoretical resolution limit of the SIMS technique and gives an upper limit of the real thickness. These SIMS measurements therefore show that dopant segregation is negligible when using boron as a dopant and the use of a locking layer is not necessary. This can be seen as a clear advantage over phosphorus since the required low temperature growth is usually associated with the formation of defects and reduced epitaxial quality of the Si overgrowth [47].
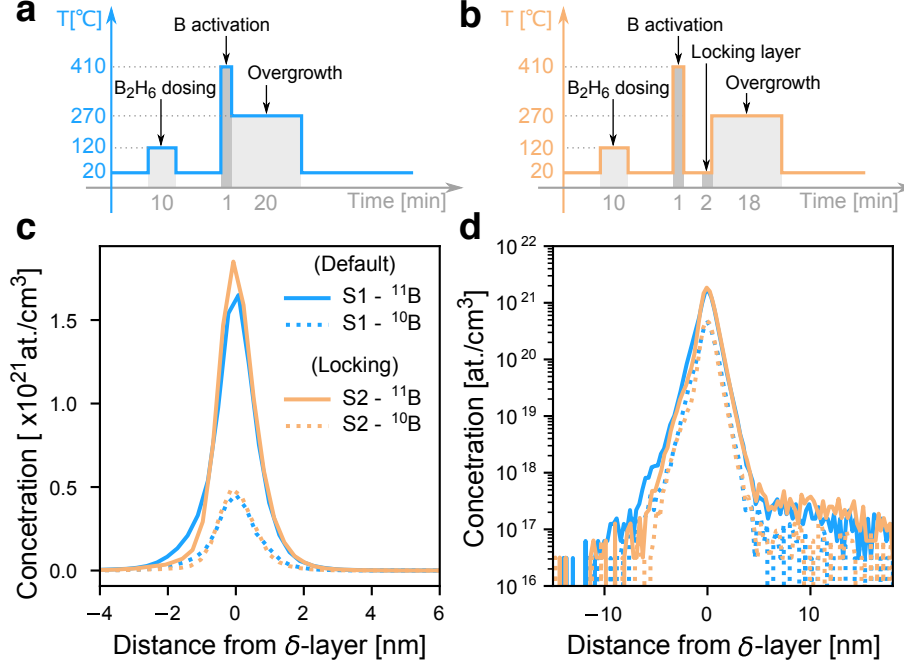
FIG. 2. | **Sample preparation and SIMS measurements of boron doped δ-layers.** **a** Preparation procedure of sample S1 (default): after dosing with diborane and a 1 min activation anneal at 410 °C the δ-layer is immediately overgrown with 20 nm of intrinsic silicon at a temperature of 275 °C. **b** In sample S2 (locking-layer) the sample is first cooled to room temperature after the activation anneal. A 2 nm thick layer of Si is grown before raising the sample temperature to 275 °C and growing the rest of the Si layer. **c**, **d** SIMS concentration profiles of the two samples: S1 (blue) and S2 (brown). Solid lines are for ^{11}B, dashed lines for ^{10}B.

Transport properties of p-type δ-layers

To study activation of the dopants we use e-beam lithography to pattern Hall bars from the δ-layer samples and anneal them at different temperatures T_A. Figure 3 **a** shows the temperature dependent resistivity per square $\rho_\square$ for a δ-layer sample with a dose of 570 L annealed for 2 min in forming gas at T_A. For a measurement temperature $T_M > 35$ K, substrate conductivity strongly influences the resistivity. Below this temperature the carriers in the low-doped substrate freeze out and the measurements reflect the properties of the boron δ-layers. In the following, only this lower temperature range is considered. $\rho_\square$ clearly drops with increasing T_A, giving values as low as 300 $\Omega \cdot \square^{-1}$ for anneals at 850 °C. For $T_A > 250$ °C the resistivities of the δ-layers show only a weak temperature dependence down

7

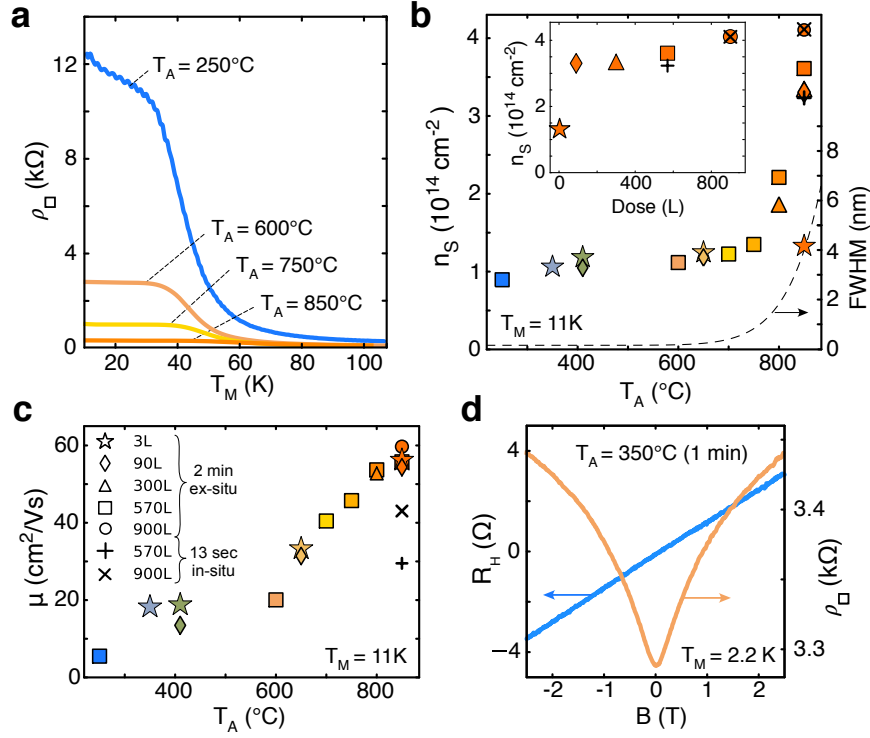FIG. 3. | **Transport properties of boron δ-layers. a** Resistivity of a 570 L δ-layer sample as a function of measurement temperature T_M annealed ex-situ at T_A for 2 min. **b** Sheet density and **c** mobility as function of annealing temperature T_A. The inset in **b** shows the weak dependence of n_S on diborane dose at $T_A = 850\,°C$. The legend for graphs **b** and **c** is given in **c**. **d** Longitudinal $\rho_\square$ and transverse R_H magnetoresistance of the 3 L sample, annealed in-situ at $T_A = 350\,°C$ for 1 min.

to $T_M = 2.2\,K$.

Figure 3 **b** shows the sheet density n_S and Figure 3 **c** the Hall mobility μ of all the samples that were investigated. Without additional annealing we find a sheet density of $10^{14} cm^{-2}$ for all samples and little changes up to $T_A = 700\,°C$. From the bulk diffusivity of boron in silicon we estimate that the full width at half the maximum of the boron distribution starts to increase at $T_A = 650\,°C$, as shown by the dashed line in Figure 3 **b** (calculated for a 2 min anneal). We find that n_S increases in sync with this broadening of the boron distribution, reaching densities as high as $4 \times 10^{14} cm^{-2}$. This corresponds to the maximum density expected from the surface reaction model put forward in Ref. [39] where BH_2 and H terminate the broken π-bond of every surface Si dimer. The observed increase in active carrier density

8

can be explained by two possible dopant (de)activation processes. First, low temperature overgrowth may leave the dopant atoms in interstitial sites or generally create crystal defects at the growth interface that deactivate a fraction of the charge carriers. However, from previous experiments with phosphorus we do not expect this to be a significant concern. The second effect is dopant deactivation because of the proximity of the boron atoms. The broadening of the δ-layer with increasing T_A leads to an increased spacing between dopants and a decrease in local density ρ_{3D}. For $T_A = 750\,°C$, we estimate $\rho_{3D} = 2\times10^{21}\text{cm}^{-3}$. At this density theoretical considerations indicate that, depending on the microscopic arrangement, only about one third of the dopants are expected to be active [48]. This is in agreement with our observations. However, it would mean that only about one boron atom per cubic Si unit cell can be active, which is significantly less than what was estimated in samples created by other techniques [49, 50]. Furthermore, it is not entirely clear why the dosing procedure we use always gives roughly the same initial density of $10^{14} cm^{-2}$ irrespective of the actual exposure dose. Contrary to what one may have expected from other STM studies [39, 40], we find no dependence on exposure dose for doses of $90\,L$ or higher after annealing at $850\,°C$ (see inset in Figure 3 **b**). The only sample which shows a sheet density that is clearly limited by the initial exposure dose is the $3\,L$ sample (filled stars).

The mobility μ is expected to be determined by ionised impurity scattering. For this situation it was discussed in Ref. [50] that μ should depend only on the active carrier concentration, similar to findings with n-type dopants. However, we find that μ increases in a more gradual fashion with T_A than the sheet density. This may indicate that disorder at the regrowth interface or clustering of the dopants within the δ-layer also play a role for μ. The fact that the $3\,L$ sample shows a slightly higher mobility for low T_A supports this, since we expect the initial dopant separation to be larger in this situation. Moreover, this sample has a factor of three lower density than the other samples at $T_A = 850\,°C$, while the mobility is again similar. In an attempt to fully activate the dopants while limiting the broadening of the δ-layer, we also performed $13\,sec$ in-situ anneals using direct current heating of two highly dosed samples at $T_A = 850\,°C$. We anneal the samples after overgrowth with $2\,nm$ of silicon and before standard encapsulation with silicon. This is indicated by the two cross symbols in Figures 3 **b**, **c**. We find that we can fully activate the dopants even though the FWHM of the dopant distribution is estimated to be only $1.4\,nm$. The mobility is, however, clearly reduced which is consistent with the expected higher value of ρ_{3D}. Note that it is

difficult to control the short duration and temperature of the anneal in-situ and we therefore expect more variability of the measured parameters for these samples.

The results from these δ-layer measurements demonstrate that full activation of the boron acceptors requires annealing temperatures $T_A > 800\,°C$. Nevertheless, it also shows that boron can be incorporated at temperatures below $450\,°C$, which is both compatible with hydrogen resist lithography and gives resistivity values $\rho_\square$ similar to those in n-type devices [37]. To support this, Figure 3 **d** shows the longitudinal magnetoresistance of the 3 L boron sample after annealing at $350\,°C$ for $1\,min$, i.e. using identical conditions as for phosphorus donor device fabrication. In contrast to phosphorus δ-layers a positive magnetoresistance is expected for boron [51] and we find a roughly four times higher $\rho_\square$, which is in equal part due to a lower μ and n_S.

p-type nanowire and gap

We combine boron p-type δ-doping with hydrogen resist lithography and create a p-type device with three terminals containing a nanowire on one side and a gap on the other. The temperatures and times used for the different steps of device fabrication are the same as in 2 **a**. A detailed description of the device fabrication process and e-beam contacting procedure can be found in Ref. [52]. The only deviation from this is the use of platinum instead of aluminium as a contact metal for p-type devices.

An STM image of the desorbed pattern before dosing with diborane is shown in Figure 4 **a** along with an outline that contains the patterned dimensions in Figure 4 **b**. Figure 4 **c** shows the electrical measurements of the gap and nanowire segment at a temperature of $4.5\,K$ (40K) for solid (dashed) lines respectively. The nanowire shows Ohmic conductivity around $0\,V$ bias while the gap only shows current after reaching a threshold voltage of about $20\,mV$, as expected for a tunnel junction. The threshold of $20\,mV$ is lower than that observed in a phosphorus device with a similar geometry [52]. Similarly, an Arrhenius fit [53] to the conductivity at zero bias (see Figure 4 **d**) gives an activation energy of $E_A = 17 \pm 5 meV$. The barrier height for a gapped wire depends on its geometry, the background doping in the substrate and the position of the Fermi energy in the impurity band in relation to the respective bulk silicon band edge [52, 54]. We speculate that the lower barrier height is due to a difference in band structure of the low-dimensional boron impurity band in the nanowire
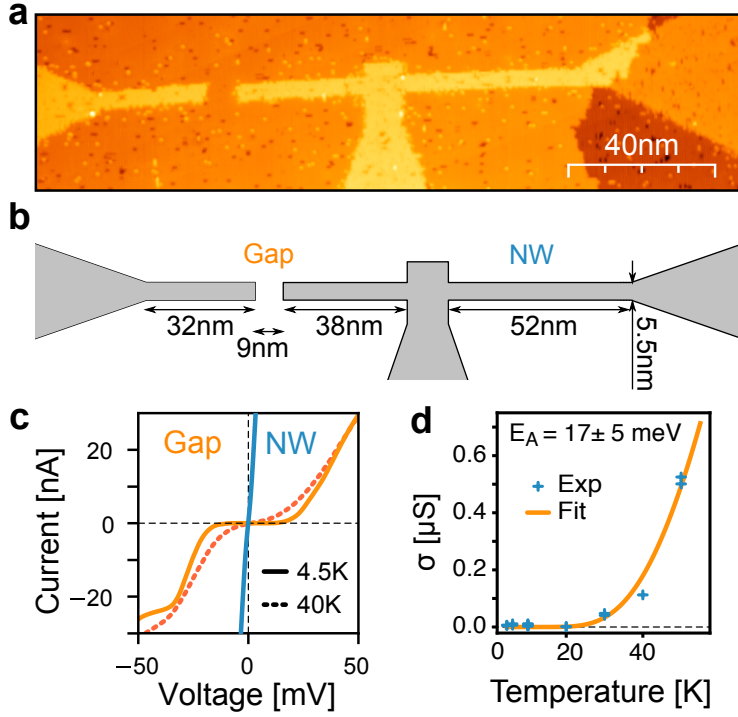
FIG. 4. | **Electrical measurements of STM defined boron doped nanowire/gap device.**
a STM image of the device after patterning of the hydrogen resist with the STM. **b** Schematic drawing of the device with dimensions **c** Current-voltage characteristics of the gap and nanowire section of the device. The dashed line shows the curve for the gap section at elevated temperature. **d** Thermally activated transport through gap section. Experimental conductance data at zero source drain bias is fit by an Arrhenius law to estimate barrier height.

contacts, however, detailed atomistic simulations would be necessary to prove this. From the resistance of the nanowire section we estimate the sheet resistivity of the boron doped layer to be $5\,\mathrm{k\Omega}\cdot\square^{-1}$.

These results show that the p-type nanowire device behaves in a similar way as expected from a corresponding n-type dopant device. The sheet resistivity of the p-type layer is slightly higher due to limited dopant activation at the temperatures available for this process. Moreover, the sheet resistivity as well as contact resistance has been more variable for p-type devices than for corresponding phosphorus doped n-type devices. The critical step is probably the activation anneal which would have to be very tightly controlled in order to achieve precisely reproducible resistivities.

pn-junction

Using both p- and n-type doping in a single sample we fabricate a two-terminal pn-junction which is the simplest bipolar device. Here, device fabrication is a two step process as outlined in Figure 5 **a**. First, we use the STM to define the areas for p-type doping, dose the sample with diborane and perform the dopant activation anneal. The reason we start with p-type doping is that the thermal budget is slightly higher and, as such, we prevent unnecessary exposure of the n-type doped areas to these higher temperatures. The temperature we use for the boron activation (410 °C) already leads to a partial desorption of the hydrogen passivation layer from the Si surface and renewal of this layer is required by exposing the sample to atomic hydrogen at a temperature of 323 °C. Subsequently, the sample is transferred back to the STM stage and hydrogen resist patterning for the n-type doping step is performed. The critical step here is alignment of the n-type pattern to the previously doped p-type area. This is achieved by careful positioning of the device within a marker pattern using an optical microscope. With a large 8×8 micron STM scan we then localise the patch with ejected silicon from the first doping step. Figure 5 **b** shows an STM image of the central part of the pn-junction after alignment and desorption of the area for n-type doping in the lower part of the pattern. The boron doped area can be seen in the upper part of the image. After STM desorption, the sample is dosed with phosphine, the activation anneal is performed and, finally, the sample is overgrown with a 20 nm thick layer of intrinsic Si. A scanning electron microscope (SEM) image of the finished pn-device is presented in Figure 5 **c**. The n- (p-type) areas show dark (bright) contrast in SEM imaging with the in-lens detector respectively. This behaviour is often observed when imaging doped semiconductors and stems from the energy sensitivity of this detector. Subsequently, the device was contacted using e-beam-defined metallic contacts and the sample was placed in a package and wire bonded.

Current-voltage characteristic of the pn-junction measured at various temperatures are shown in Figures 5 **d**, **e**. The pn-junction is expected to exhibit asymmetric behaviour with higher conductivity in the forward direction (positive voltage). This behaviour can be seen for voltages higher than ∼0.6 V (region 5 in Figure 5 **d**). For the reverse-bias direction (negative voltage) we can see a more gradual increase of the current (region 1). This is related to the high doping density on both sides of the pn-junction - the depletion region

12

in this regime is narrow and allows inter-band-tunneling of the charge carriers. In region 2 near zero applied bias voltage the current is suppressed, which is different from conventional highly doped pn-junctions (Esaki diodes). There are several possible reasons for this: First, differences in the band structure of the p-type and n-type 2D δ-layers could lead to current suppression in this low bias regime. Second, the two degenerately doped contacts of the tunneling device are in-plane which will impact the electrostatics that determine the size of the depletion region. Third, the boron doped side is expected to have a significant amount of deactivated dopants which will impact device performance and may lead to localisation effects at low voltage bias. To fully determine the origin of this suppression will require detailed modelling of the device which is beyond the scope of this paper. In region 3, at slightly larger bias, the current increases up to a peak value I_P. Here inter-band-tunneling dominates transport in the forward direction. At even larger bias voltage, tunneling is suppressed by a misalignment of the bands in the p- and n-doped regions which leads to negative differential resistance and a current minimum I_V. This region of negative differential resistance is a characteristic feature for Esaki diodes and a typical figure of merit is the so called peak to valley current ratio $I_P/I_V \approx 1.7 \pm 0.1$. This is lower than that of conventional bulk silicon tunnel diodes [55] but is strongly impacted by the suppression of the current in region 2. In region 5 intra-band current flow becomes possible in the forward direction and a steep increase is observed. The position of this rapid rise shifts to lower bias voltages as temperature is increased in agreement with expectations for an Esaki diode. Moreover, conduction in region 2 is also strongly temperature dependent. At the highest temperature $T = 34$ K, bulk conductivity through the enclosing substrate starts to play a role and the negative differential resistance disappears.

Fabrication of bipolar devices is not substantially more demanding than fabrication of an n- or p-type dopant device. The only additional step is the alignment of the STM tip to the previously doped region and this can be solved by choosing a device position that is easy to locate with respect to the optical localisation markers. However, similarly to the remark about p-type devices in the previous section, there is larger variability in the sheet resistivities and contact resistances. For a number of pn-devices we even encountered issues with non-functional contacts, mostly to the p-type part of the device. We believe that these problems can be solved by better control of the boron activation step, however, this will require more detailed investigation before the technique can be adapted as a routine
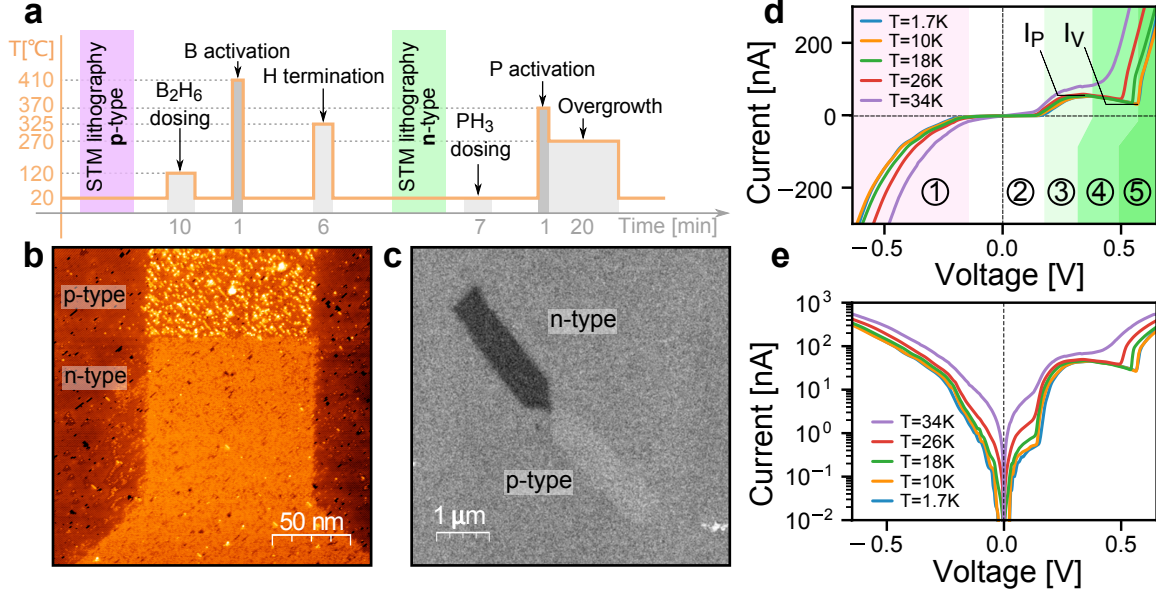
FIG. 5. | **Fabrication of a bipolar dopant device with STM lithogrpahy. a** Preparation procedure, **b** STM image of the central part of the pn-junction after desorption of the area for phosphorus doping (lower part). In the upper section, the boron doped and incorporated area is visible. **c** Ex-situ SEM image of the pn-device from **c**. Linear **d** and semilogarithmic plot of the current-voltage characteristics of the pn-junction as a function of temperature.

method for bipolar dopant device fabrication.

CONCLUSIONS

We have shown that hydrogen-resist lithography with the tip of an STM can be used to pattern p-type nanostructures with an indicated resolution better than $2\,\text{nm}$. Though full activation of the dopants can only be reached at $T_A = 850\,^\circ\text{C}$, we demonstrate that boron δ-layers with resistivities below $3.3\ \text{k}\Omega \cdot \square^{-1}$ can be fabricated using incorporation temperatures that are compatible with hydrogen resist lithography. To illustrate the capabilities of the approach, we fabricated a 5.5-nm-wide p-type dopant nanowire, which shows ohmic conductivity and resistivity of about $5\,\text{k}\Omega \cdot \square^{-1}$. By combining the p-type doping with established n-type doping, we also fabricate a bipolar dopant device — a $100\,\text{nm}$-wide pn-junction, which behaves similar to an Esaki diode. Our approach could be used to fabricate a large variety of more complex p-type and bipolar nanoscale dopant devices.

14

METHODS

Samples are fabricated from $2.7 \times 9\,\text{mm}$, n-type Si(001) wafer pieces with a resistivity of $0.1\text{-}1.0\,\Omega\,\text{cm}$. For sample preparation and hydrogen passivation we follow the procedure outlined in Ref. [56].

For desorption of hydrogen with the STM tip we typically used a tunneling current setpoint of $3\,\text{nA}$ and sample bias of $+4.1\,\text{V}$ (for high resolution patterning of nanoscale parts) up to $6.5\,\text{V}$ (for fast low resolution desorption of large areas).

Scale bars in high resolution STM images were calibrated from the average spacing of Si dimer rows where visible. In all other pictures the original scale bar from the imaging instrument was used.

Dopant pre-cursors are introduced through a leak valve directly into the STM chamber containing an Omicron VT STM/AFM system. For diborane dosing we use 30% diborane in molecular hydrogen (H_2). The sample is positioned directly in the gas flux while maintaining constant pressure in the chamber. The doses given refer to total gas exposure as calculated from chamber pressure multiplied by exposure time. This means that effective diborane doses are about a factor of three lower than what we state.

Silicon overgrowth is performed by sublimation from an intrinsic silicon filament with a typical rate of 0.4 nm/min while keeping the sample at $270\,^\circ\text{C}$. After this, further processing occurs ex-situ using standard lithography techniques. For contacting the p-type devices we used Pt contacts, since the Fermi level in Pt is closer to that of degenerately doped p-type Si leading to a lower Schottky barrier. In the case of bipolar devices, we used Al contacts.

The SIMS profiles (Cameca SC Ultra) have been acquired using a $250\,\text{eV}$ O_2^+ primary beam with an incidence angle of 46° to the sample normal (calculated based on the potentials).

The boron concentration in the SIMS profiles was quantified by measuring a boron reference sample with a known boron concentration and by applying the RSF method point-by-point relative to the Si matrix signal. The total crater depth of the reference sample was measured by stylus profilometry allowing determination of the current-normalised sputter rate value. This value was then applied point-by-point to all profiles relative to their primary current curves to account for sputter rate variations with the primary beam current.

DATA AVAILABILITY

The data that support the findings of this study (STM images, raw measurement data, raw SIMS data) are available through Zenodo at https://doi.org/10.5281/zenodo.3881492 Further information is available from the corresponding author upon reasonable request.

───────────

* afu@zurich.ibm.com

[1] Frank, D. *et al.* Device Scaling Limits of Si MOSFETs and Their Application Dependencies. *Proceedings of the IEEE* **89**, 259 – 288 (2001).

[2] Ho, J. *et al.* Controlled nanoscale doping of semiconductors via molecular monolayers. *Nat. Mater.* **7**, 62–67 (2008).

[3] Colombeau, B. *et al.* Advanced CMOS devices: Challenges and implant solutions. *Phys. Stat. Sol. (a)* **211**, 101–108 (2014).

[4] Duffy, R. *et al.* Access resistance reduction in Ge nanowires and substrates based on non-destructive gas-source dopant in-diffusion. *J. Mat. Chem. C* **2**, 9248–9257 (2014).

[5] Muhonen, J. *et al.* Storing quantum information for 30 seconds in a nanoelectronic device. *Nat. Nanotechnol.* **9**, 986–991 (2014).

[6] Roche, B. *et al.* A two-atom electron pump. *Nat. Commun.* **4**, 1581 (2013).

[7] Schofield, S. *et al.* Atomically Precise Placement of Single Dopants in Si. *Phys. Rev. Lett.* **91**, 136104 (2003).

[8] Fuechsle, M. *et al.* A single-atom transistor. *Nat. Nanotechnol.* **7**, 242–246 (2012).

[9] Simmons, M. *et al.* Scanning probe microscopy for silicon device fabrication. *Mol. Simul.* **31**, 505–514 (2005).

[10] van der Heijden, J. *et al.* Probing the Spin States of a Single Acceptor Atom. *Nano Lett.* **14**, 1492–1496 (2015).

[11] Wang, Y., Shan, J. & Hamers, R. J. Combined scanning tunneling microscopy and infrared spectroscopy study of the interaction of diborane with Si(001). *J. Vac. Sci. Techn. B* **14**, 1038–1042 (1996).

[12] L.Yu, M., Vitkavage, D. & Meyerson, B. Doping reaction of PH_3 and B_2H_6 with Si(100). *J. Appl. Phys.* **59**, 4032–4037 (1986).

[13] Oura, K. *et al.* Hydrogen adsorption on Si(100)-2x1 surfaces studied by elastic recoil detection analysis. *Phys. Rev. B* **41**, 1200–1203 (1990).

[14] Dürr, M., Hu, Z., A., B., U., H. & Heinz, T. Real-Space Study of the Pathway for Dissociative Adsorption of H_2 on Si(001). *Phys. Rev. Lett.* **88**, 046104 (2002).

[15] Wang, Y. & Hamers, R. Boron-induced reconstructions of Si(001) investigated by scanning tunneling microscopy. *J. Vac. Sci. Technol. A* **13**, 1431–1437 (1995).

[16] Wilson, H. *et al.* Thermal dissociation and desorption of PH_3 on Si(001): A reinterpretation of spectroscopic data. *Phys. Rev. B* **74**, 195310 (2006).

[17] Liu, Z., Zhang, Z. & Zhu, X. Atomic structures of boron-induced protrusion features on Si(100) surfaces. *Phys. Rev. B* **77**, 035322 (2008).

[18] Goh, K., Oberbeck, L., Simmons, M., Hamilton, A. & Clark, R. Effect of encapsulation temperature on Si:P δ -doped layers. *Appl. Phys. Lett.* **85**, 4953–4955 (2004).

[19] Keizer, J., Koelling, S., Koenraad, P. & Simmons, M. Suppressing Segregation in Highly Phosphorus Doped Silicon Monolayers. *ACS Nano* **9**, 12537–12541 (2015).

[20] Luo, X., Zhang, S. & Wei, S.-H. Understanding Ultrahigh Doping: The Case of Boron in Silicon. *Phys. Rev. Lett.* **90**, 026103 (2003).

[21] Bustarret, E. *et al.* Superconductivity in doped cubic silicon. *Nature* **444**, 465–468 (2006).

[22] Weir, B. *et al.* Electrical characterization of an ultrahigh concentration boron delta-doping layer. *Appl. Phys. Lett.* **65**, 737–739 (1994).

[23] Dai, P., Zhang, P. & Sarachik, M. Electrical conductivity of metallic Si:B near the metal-insulator transition. *Phys. Rev. B* **45**, 3984–3994 (1992).

[24] Pascher, N., Hennel, S., Mueller, S. & Fuhrer, A. Tunnel barrier design in donor nanostructures defined by hydrogen-resist lithography. *New J. Phys.* **18**, 083001 (2016).

[25] Arrhenius, S. Über die Reaktionsgeschwindigkeit bei der Inversion von Rohrzucker durch Säuren. *Z. Phys. Chem.* **4**, 226–248 (1889).

[26] Ryu, H. *et al.* Atomistic modeling of metallic nanowires in silicon. *Nanoscale* **5**, 8666–8674 (2013).

[27] Oehme, M. *et al.* Si Esaki diodes with high peak to valley current ratios. *Appl. Phys. Lett.* **95**, 242109–242111 (2009).

[28] Fuhrer, A., Füchsle, M., Reusch, T., Weber, B. & Simmons, M. Atomic-Scale, All Epitaxial In-Plane Gated Donor Quantum Dot in Silicon. *Nano Lett.* **9**, 707–710 (2009).

[29] Frank, D. *et al.* Device Scaling Limits of Si MOSFETs and Their Application Dependencies. *Proceedings of the IEEE* **89**, 259 – 288 (2001).

[30] Ho, J. *et al.* Controlled nanoscale doping of semiconductors via molecular monolayers. *Nat. Mater.* **7**, 62–67 (2008).

[31] Colombeau, B. *et al.* Advanced CMOS devices: Challenges and implant solutions. *Phys. Stat. Sol. (a)* **211**, 101–108 (2014).

[32] Duffy, R. *et al.* Access resistance reduction in Ge nanowires and substrates based on non-destructive gas-source dopant in-diffusion. *J. Mat. Chem. C* **2**, 9248–9257 (2014).

[33] Muhonen, J. *et al.* Storing quantum information for 30 seconds in a nanoelectronic device. *Nat. Nanotechnol.* **9**, 986–991 (2014).

[34] Roche, B. *et al.* A two-atom electron pump. *Nat. Commun.* **4**, 1581 (2013).

[35] Schofield, S. *et al.* Atomically Precise Placement of Single Dopants in Si. *Phys. Rev. Lett.* **91**, 136104 (2003).

[36] Fuechsle, M. *et al.* A single-atom transistor. *Nat. Nanotechnol.* **7**, 242–246 (2012).

[37] Simmons, M. *et al.* Scanning probe microscopy for silicon device fabrication. *Mol. Simul.* **31**, 505–514 (2005).

[38] van der Heijden, J. *et al.* Probing the Spin States of a Single Acceptor Atom. *Nano Lett.* **14**, 1492–1496 (2015).

[39] Wang, Y., Shan, J. & Hamers, R. J. Combined scanning tunneling microscopy and infrared spectroscopy study of the interaction of diborane with Si(001). *J. Vac. Sci. Techn. B* **14**, 1038–1042 (1996).

[40] L.Yu, M., Vitkavage, D. & Meyerson, B. Doping reaction of PH_3 and B_2H_6 with Si(100). *J. Appl. Phys.* **59**, 4032–4037 (1986).

[41] Oura, K. *et al.* Hydrogen adsorption on Si(100)-2x1 surfaces studied by elastic recoil detection analysis. *Phys. Rev. B* **41**, 1200–1203 (1990).

[42] Dürr, M., Hu, Z., A., B., U., H. & Heinz, T. Real-Space Study of the Pathway for Dissociative Adsorption of H_2 on Si(001). *Phys. Rev. Lett.* **88**, 046104 (2002).

[43] Wang, Y. & Hamers, R. Boron-induced reconstructions of Si(001) investigated by scanning tunneling microscopy. *J. Vac. Sci. Technol. A* **13**, 1431–1437 (1995).

[44] Wilson, H. *et al.* Thermal dissociation and desorption of PH_3 on Si(001): A reinterpretation of spectroscopic data. *Phys. Rev. B* **74**, 195310 (2006).

[45] Liu, Z., Zhang, Z. & Zhu, X. Atomic structures of boron-induced protrusion features on Si(100) surfaces. *Phys. Rev. B* **77**, 035322 (2008).

[46] Goh, K., Oberbeck, L., Simmons, M., Hamilton, A. & Clark, R. Effect of encapsulation temperature on Si:P δ -doped layers. *Appl. Phys. Lett.* **85**, 4953–4955 (2004).

[47] Keizer, J., Koelling, S., Koenraad, P. & Simmons, M. Suppressing Segregation in Highly Phosphorus Doped Silicon Monolayers. *ACS Nano* **9**, 12537–12541 (2015).

[48] Luo, X., Zhang, S. & Wei, S.-H. Understanding Ultrahigh Doping: The Case of Boron in Silicon. *Phys. Rev. Lett.* **90**, 026103 (2003).

[49] Bustarret, E. *et al.* Superconductivity in doped cubic silicon. *Nature* **444**, 465–468 (2006).

[50] Weir, B. *et al.* Electrical characterization of an ultrahigh concentration boron delta-doping layer. *Appl. Phys. Lett.* **65**, 737–739 (1994).

[51] Dai, P., Zhang, P. & Sarachik, M. Electrical conductivity of metallic Si:B near the metal-insulator transition. *Phys. Rev. B* **45**, 3984–3994 (1992).

[52] Pascher, N., Hennel, S., Mueller, S. & Fuhrer, A. Tunnel barrier design in donor nanostructures defined by hydrogen-resist lithography. *New J. Phys.* **18**, 083001 (2016).

[53] Arrhenius, S. Über die Reaktionsgeschwindigkeit bei der Inversion von Rohrzucker durch Säuren. *Z. Phys. Chem.* **4**, 226–248 (1889).

[54] Ryu, H. *et al.* Atomistic modeling of metallic nanowires in silicon. *Nanoscale* **5**, 8666–8674 (2013).

[55] Oehme, M. *et al.* Si Esaki diodes with high peak to valley current ratios. *Appl. Phys. Lett.* **95**, 242109–242111 (2009).

[56] Fuhrer, A., Füchsle, M., Reusch, T., Weber, B. & Simmons, M. Atomic-Scale, All Epitaxial In-Plane Gated Donor Quantum Dot in Silicon. *Nano Lett.* **9**, 707–710 (2009).

ACKNOWLEDGEMENTS

AUTHOR CONTRIBUTIONS

A.F. designed the study and directed the project. S.A.K., A.F. developed the diborane doping procedures, fabricated and measured the Hall bar devices, S.A.K., T.S., A.F. developed the diborane lithography process, A.F., T.S. designed, fabricated and measured the STM patterned devices. B.D, C.F., T.S. performed the SIMS experiments and analysed the SIMS data. T.S., A.F., S.A.K analysed the device data and wrote the manuscript with contributions from all authors.